PCCP

PAPER

View Article Online
View Journal | View Issue

Cite this: *Phys. Chem. Chem. Phys.*, 2023, **25**, 9176

Satellite ligand effects on magnetic exchange in dimers. A structural, magnetic and theoretical investigation of $Cu_2L_2X_4$ (L = methylisothiazolinone and X = Cl^-, Br^-)†

Stefan Coetzee,[a] Mark M. Turnbull,[b] Christopher P. Landee,[c] Jeffrey C. Monroe,[b] Mercè Deumal,[d] Juan. J. Novoa[e] and Melanie Rademeyer *[a]

Received 2nd December 2022,
Accepted 27th February 2023

DOI: 10.1039/d2cp05629a

rsc.li/pccp

Halide-bridged polymers have gained significant interest due to their diverse properties and potential applications. Stacked $Cu_2L_2X_4$ dimers, where L is an organic ligand and X can be Cl^- or Br^-, are of interest because a chloride analogue where L = 2-pyridone, had previously been reported to exhibit bulk ferromagnetism, which augured great potentiality for this class of compounds. The synthesis, structural characterization, magnetic susceptibility measurements, and computational studies of two isostructural **CuClMI** (MI = methylisothiazolinone) and **CuBrMI** polymers of Cu(II), along with a related **CuClPYR** (PYR = 2-pyridone) is reported. **CuClMI** and **CuBrMI** were found to exhibit AFM bulk properties, due to FM/AFM alternating chains along the halide-bridged polymer axis, while FM bulk properties were confirmed for **CuClPYR** exhibiting a FM spin ladder. In combination with a benzamide analogue, **CuClBA**, three O-donor amides, **CuClMI**, **CuClBA** and **CuClPYR** were analyzed and revealed that the kinetic exchange is affected by the identity, but more importantly, the orientation of the satellite ligands. The torsional angle of the ligand with the dimer plane is shown to significantly affect the magnetic exchange in the dimer, and between dimers, explaining the reported FM bulk properties of **CuClPYR**. This finding is exceedingly important, as it suggests that a spin device can be constructed to flip between singlet/triplet states by manipulating the orientation of the satellite/terminal ligand.

Introduction

Halide-bridged polymers of Cu(II) are known to exhibit a myriad of structural permutations. Selected examples of common halide-bridged polymers are illustrated in Scheme 1. Of specific interest in the current study are double-halide-bridged polymers (Scheme 1(d)) consisting of stacked, planar dimers of the formula $Cu_2L_2X_4$, where L is an organic ligand, and X = Cl^- or Br^-, as depicted in Fig. 1.

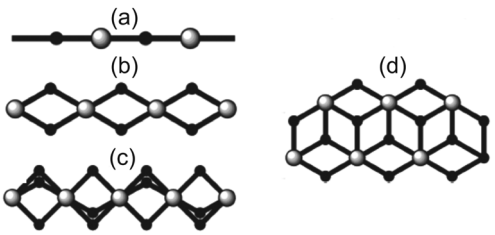

Scheme 1 Examples of different types of halide-bridged polymers are (a) corner-sharing, (b) simple edge-sharing, (c) face-sharing, and (d) complex edge-sharing. Black and white spheres represent transition metals and halide ligands respectively.

The current study will focus on the magnetic properties of stacked-dimer halide-bridged polymers that form low-dimensional magnetic materials as a result of the presence of the inorganic polymer in the structure, with the bridging halide ions resulting in various Cu–X···X–Cu and Cu–X···Cu magnetic

[a] *Department of Chemistry, University of Pretoria, Pretoria, 0002, South Africa. E-mail: melanie.rademeyer@up.ac.za*
[b] *Carlson School of Chemistry and Biochemistry, Clark University, 950 Main St., Worcester, Massachusetts, 01610, USA*
[c] *Department of Physics, Clark University, 950 Main St., Worcester, Massachusetts, 01610, USA*
[d] *Serra-Húnter Fellow, Departament de Ciència de Materials i Química Física and IQTCUB, Facultat de Química, Universitat de Barcelona, Martí i Franquès 1, 08028, Barcelona, Spain*
[e] *Departament de Ciència de Materials i Química Física and IQTCUB, Facultat de Química, Universitat de Barcelona, Martí i Franquès 1, 08028, Barcelona, Spain*

† Electronic supplementary information (ESI) available: Crystallographic data and powder X-ray diffraction patterns; dimer and tetramer cluster models; discussion of magnetic models and their calculated magnetic susceptibility; decomposition of J_{AB}; analysis of **CuClPYR**; spin densities and SOMO's for dimer magnetic models; calculation of magnetic properties of **CuClMI**; comparison of magnetic data for **CuClMI**; energy spectra and thermal population. CCDC 2191590. For ESI and crystallographic data in CIF or other electronic format see DOI: https://doi.org/10.1039/d2cp05629a

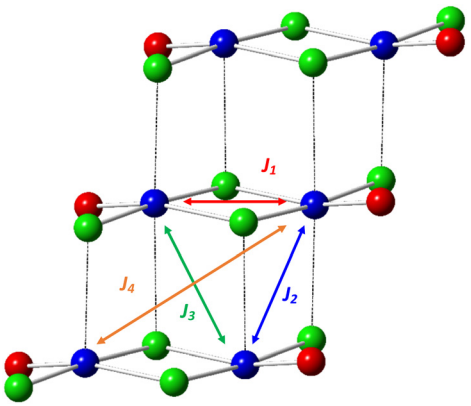

Fig. 1 Stacked dimers in Cu(II)-based halide bi-bridged compounds, whose magnetic interactions can potentially occur within the dimer (J_1), or *via* interactions between dimers (J_{2-4}). Colour code: Cu in blue, X in green, L in red, where X = Cl^- or Br^- and L = organic ligand.

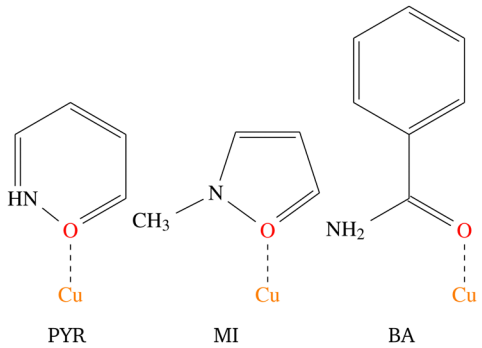

Scheme 2 The structures of the three amides, 2-pyridone (PYR), methylisothiazolinone (MI) and benzamide (BA) ligands considered in this study, with the coordination modes indicated.

Table 1 Relevant intra- (Cu···Cu in-plane) and inter-dimer (Cu···Cu out of plane) J_{AB} magnetic couplings in $Cu_2X_2L_2$ stacked-dimer polymers, where X = Cl^- or Br^- and L = BA, MI or PYR (all J_{AB} values in cm^{-1}). Values for **CuXBA** were calculated at UB3LYP/TZVP level.[6] Values for **CuClMI** and **CuClPYR** from fitting of experimental data[2,7]

	J_1[a]	J_2[b]	J_3[b]
CuClBA[6]	34.7	0.3	−3.32
CuClMI[2]	5.03	1.96	−1.36
CuClPYR[7]	9.4	−3.2	
CuBrBA[6]	49.67	∼0.30	−7.15

[a] Intra-dimer coupling. [b] Inter-dimer coupling.

exchange pathways between Cu(II) cations. Low-dimensional magnetic materials are of interest in the modeling and understanding of room-temperature superconductors[1] and can assist in the fundamental understanding of magneto-structural relationships. In addition, the Cu(II) ion represents a simple magnetic ion, with $S = 1/2$ and quenching of the orbital angular momentum. This makes it an ideal system to study both experimentally and computationally. The magnetic exchange interactions in these stacked-dimer halide-bridged polymers have been the subject of several studies reported in the literature, with different magnetic properties reported for polymers containing different organic ligands.[2–5] The parent compound, $CuCl_2$, has been found to exhibit incommensurate long-range magnetic phase transitions at low temperatures into an antiferromagnetic (AFM) spin spiral.[8] and have been shown to be sensitive to the nature of the halide, and geometric parameters of the inorganic bridge.[9] Rodríguez *et al.*[10] studied multiple parameters' effects on the magnetic exchange in polymeric $(Cu_2X_2(NH_3)_4)^{2+}$ dimers through the use of density functional theory (DFT). They demonstrated that the magnetic exchange was determined by the way the Cu(II) ions were linked, including the connectivity, bond angles, bond lengths, and variation in the bridging geometry, but of more interest in this context, that the type of ligand attached to the terminal positions of the polymers (red atoms in Fig. 1) have a large influence on the magnitude and sign of the magnetic exchange in these dimers. Cl^- terminal ligands favored AFM exchange across the dimers, while N-donor ligands favored FM exchange. Importantly, their work focussed on the dimers in isolation, only considering the magnetic exchange in the dimer (blue arrow in Fig. 1). Coetzee *et al.* demonstrated that the magnetic exchange of these compounds is actually determined by the inter-dimer exchange (green arrow in Fig. 1) if the exchange across the dimer is FM.[6] Inspired by the abovementioned contributions, the current authors examined a related set of **CuXL** compounds,[6] where X = Cl^- or Br^- and L = O-donor amides, shown in Scheme 2. The Heisenberg Hamiltonian used throughout all studies is of the form: $\hat{H} = -2\sum J_{AB}\hat{S}_A \cdot \hat{S}_B$ where positive J_{AB} corresponds to a FM interaction. When the amide is benzamide (BA), the exchange in the dimers (J_1) was found to be strongly FM (red arrow for Cu···Cu in-plane magnetic exchange in Fig. 1) with $J_1^{CuClBA} = +34.70\ cm^{-1}$ and $J_1^{CuBrBA} = +49.67\ cm^{-1}$. Dimers had very small FM ($\sim 0.3\ cm^{-1}$) inter-dimer interactions (blue (J_2) and orange (J_4) arrows in Fig. 1) competing with stronger AFM inter-dimer interactions (green arrows in Fig. 1) of $J_3^{CuClBA} = -3.32\ cm^{-1}$ and $J_3^{CuBrBA} = -7.15\ cm^{-1}$ (see Table 1) resulting in an 1D magnetic topology, which consists of alternating chains of FM dimers (effective $S = 1$) antiferromagnetically connected. When the amide is 2-pyridone (PYR), J_1 was experimentally fitted to be weakly FM ($+9.4\ cm^{-1}$), with the overall exchange between dimers AFM ($-3.2\ cm^{-1}$) for **CuClPYR**, resulting in an overall FM low-temperature response.[7] The authors did comment that the model did not fit well, which may indicate that the magnetic structure of **CuClPYR** is more complex. When the amide is methylisothiazolinone (MI), the fitted magnetic exchange of **CuClMI** was reported to have a FM J_1 of $+5.03\ cm^{-1}$, a FM $J_2 = +1.96\ cm^{-1}$ and an AFM J_3 of $-1.36\ cm^{-1}$ resulting in an overall FM response.[2]

Therefore, when the amide is MI and PYR, the bulk properties are FM, while BA produces AFM bulk properties at low temperatures. J_1 is FM in all cases, while J_2 and J_3 vary significantly. This is interesting since all of the terminal ligands are similar and is even more intriguing when comparing the structures of the bridges, where differences in the Cu–Cl distances are all within 0.01 Å, Cu···Cl distances within 0.05 Å,

Cl–Cu···Cl and Cu–Cl···Cu angles are within 1° respectively, while the interdimer Cu–Cl···Cu angles are within 2° of one another. The inorganic polymer backbone, is, therefore effectively the same for **CuClBA**, **CuClMI**, and **CuClPYR**. Yet, these compounds produce different magnetic properties.

The differentiating structural feature between these three compounds is the Cl_{term}–Cu–O–$C_{carbonyl-C}$ torsional angle, which are 135°, 55° and 58° for **CuClPYR**, **CuClMI**, and **CuClBA**, respectively. **CuClMI**, as we will show, actually exhibits AFM properties, similar to **CuClBA**, which points to the Cl_{term}–Cu–O–$C_{carbonyl-C}$ torsional angle as the parameter that has an effect on one or more of the exchange interactions that results in the different observed properties.

To understand how this occurs, a computational study using the First-Principles Bottom-Up (FPBU)[11] method, and other calculations were conducted on **CuClMI**, **CuClBA**, **CuClPYR**, and the newly synthesized **CuBrMI** compound. The calculated J_i values are validated against experimental data, and a rigorous magnetic model is obtained for these compounds. It must be stressed that the effect of coordination angle on individual magnetic exchange interactions is explored as a target for spin manipulation.

Experimental section

Chemicals and reagents

All chemicals were used as purchased without further purification: $CuBr_2$ (99%, Sigma Aldrich), 2-methyl-1,2-thiazol-3(2*H*)-one (methylisothiazolinone) (99%, Aldrich), ethanol (99.8%, Sigma-Aldrich).

Synthesis of di-bromo-bis[bromo(methylisothiazolinone) copper(II)], CuBrMI. $CuBr_2$ (0.5398 g, 2.417 mmol) was dissolved in 40 ml ethanol. To this solution, methylisothiazolinone (0.2783 g, 2.418 mmol) was added dropwise. On standing at room temperature, open to the atmosphere, crystals of the brown product began to form after approximately an hour. The crystals were filtered off and a good quality crystal was selected for the single-crystal X-ray diffraction study. Single crystals were ground to a fine powder to provide a sample for powder X-ray diffraction and magnetic analysis. No attempts were made to optimize the yield. Yield: 12.77%. [9.937 mg] elemental analysis: calculated: C: 14.19%, H: 1.49%, N: 4.14%; found: C: 14.21%, H: 1.58%, N: 4.01%.

Synthesis of di-chloro-bis[chloro(methylisothiazolinone) copper(II)], CuClMI. 0.6761 g (5.029 mmol) $CuCl_2$ was dissolved in 20 ml of ethanol. To this solution, 0.5893 g (5.120 mmol) methylisothiazolinone was added dropwise. On standing at room temperature, open to the atmosphere, the crystals of the orange product started to precipitate immediately. The crystals were filtered off. Single crystals were ground to a fine powder to provide a sample for powder X-ray diffraction and magnetic analysis. No attempts were made to optimize the yield. Yield: 47.36%. [7.717 mg] elemental analysis: calculated: C: 19.25%, H: 2.02%, N: 5.61%; found: C: 18.96%, H:2.05%, N: 5.51%.

Data acquisition

The structure of **CuClMI** was published by Kato *et al.*[2] and the structure files were obtained from the Cambridge Structural Database (CSD)[12] with the CSD refcode: [OPABAJ],[2] which was used as the input structure for the computational investigation. An experimental magnetic susceptibility data set for **CuClMI** was obtained from the original author, M. Kato.[2]

Instrumental studies

Single crystal X-ray diffraction. X-ray diffraction data were collected on a Bruker D8 Venture diffractometer, with a Photon 100 CMOS detector, at 150(2) K, employing a combination of ϕ and ω scans. Monochromatic MoK-α radiation of wavelength 0.71073 Å, from an *I*μs source, was employed as irradiation source. Cooling was achieved using an Oxford Cryogenics Cryostat. Data reduction were performed using the software SAINT+[13] and absorption corrections were performed using SADABS[14] as part of the APEXII[15] suite. The crystal structure of **CuBrMI** was solved by intrinsic phasing using SHELX-2018,[16] as part of the WinGX suite.[17] Structure refinement was done using SHELXL[18] in WinGX as GUI. Graphics and publication material were generated using Mercury 3.10[19] and Crystalmaker 9.[20] All hydrogen atoms were placed as observed in the difference map and refined isotropically in the **CuBrMI** structure.

Powder X-ray diffraction. The powder X-ray diffraction patterns of **CuClMI** and **CuBrMI** were collected on a Bruker D2 Phaser powder diffractometer using a low-background Si sample holder, at room temperature. The experimental powder patterns were compared with the powder patterns calculated from single crystal structure data using the software DiffractWD[21] (Section S1, ESI†).

Experimental magnetic data. Magnetic data for **CuClMI** and **CuBrMI** were measured using a Quantum Design MPMS-XL SQUID magnetometer. A finely ground powder sample of **CuClMI** (33.4 mg) or **CuBrMI** (82.9 mg) was packed into a gelatine capsule and placed into a plastic straw. A second 37.7 mg sample of **CuClMI** was also characterised to confirm an observed anomaly at 15 K. Magnetic analysis entailed the measurement of magnetisation as a function of an applied field ranging from 0 to 50 KOe, and the measurement of selected points on returning the field to zero, to monitor for hysteresis effects, which were not observed. The data were linear to 10 kOe for **CuBrMI** and 20 kOe for **CuClMI**. Magnetic susceptibility was measured between 1.8 K and 310 K in an applied field of 1 kOe for both samples. The measured data were corrected for diamagnetic contributions from the atoms comprising the compound using Pascal's constants, for the background of an empty gelatin capsule, measured independently, and the temperature-independent paramagnetism of a Cu(II) ion. A comparison of the experimental powder X-ray diffraction patterns of the samples that were used for the magnetic studies with the powder pattern simulated from the single crystal X-ray diffraction structure of **CuBrMI** and **CuClMI** confirmed the phase purity of the powder samples (Section S1, ESI†).

Computational details

The First Principles Bottom-Up (FPBU)[11] working strategy allows for a systematic theoretical analysis of the magnetic topology and the calculation of the bulk magnetic properties of a material. The only input into the analysis is the experimental single-crystal structure. The FPBU analysis was completed for **CuClMI**,[2] **CuClPYR**,[7] and the new crystal structure of **CuBrMI** determined in this study.

Potential pairs of radicals are identified from the crystal structure, up to a cut-off distance of *ca.*10 Å between Cu(II) ions. Once all the radical pairs have been identified, the radical···radical pair magnetic exchange interactions (J_{AB}) for all the unique radical pairs are calculated. Cluster models used to evaluate magnetic coupling between Cu-moieties must account for the coordination and environment of both Cu(II) ions, *i.e.* for X and L ligands in **CuXL** compounds. Using the Heisenberg Hamiltonian $\hat{H} = -2\sum J_{AB}\hat{S}_A \cdot \hat{S}_B$ and broken-symmetry (BS) approximation,[22] the magnetic exchange interaction J_{AB} between any two radicals A and B is calculated at the level of unrestricted density functional theory (DFT/UB3LYP)[23–26] through the difference in energy between the triplet (E_T) and open-shell singlet state using the broken-symmetry approach (E_S^{BS}) employing a dimer cluster model (see eqn (1)).

$$\Delta E^{S-T} = E_S - E_T = \frac{2\left(E_S^{BS} - E_T\right)}{1 + {S_{ab}}^2} = 2J_{AB} \qquad (1)$$

In eqn (1), S_{ab} represents the overlap between molecular spin-carrying orbitals and is obtained from the DFT calculations, to produce spin-projected energy for the BS state. This approximation can be extended to cluster models containing more than two radicals, which generally improves the description of the chemical environment around the radicals and provide a more accurate estimation of J_{AB} (see ESI,† Section S2 for a detailed discussion). For this work, a finite cluster comprised of two stacked $Cu_2L_2X_4$ dimeric units (tetramer model) was used in addition to the dimer model, where several spin permutations were calculated to determine the individual J_{AB} values. The dimer and tetramer finite cluster models were required to calculate the different J_{AB} values for all compounds (hereafter, J_i). All energies were calculated using the Ahlrich TZVP basis set.[27] The energy calculations for the pairs of radical dimers were carried out using Gaussian 09 Rev. D01,[28] and for the tetrameric structures, ORCA 4.2.0[29] was used.

Based on the value of the significant J_i interactions, a magnetic topology is constructed, and magnetic models extracted accordingly. It must be stressed that a good magnetic model, in addition to include the most relevant J_i interactions, should have topological connectivity similar to the bulk of the material. Therefore, from the diagonalization of the appropriate magnetic model, the energy eigenvalues and the total spin number of each respective state are determined. No interactions are excluded *a priori* and multiple arrangements and connectivities are tested to obtain a model that best mimics the experimental data. A good model should display a convergence toward the experimental values as the number of radicals is increased, for example, from 2 to 8 to 16, in the effective Hamiltonian (see Section S3 for further discussion, ESI†).

Finally, the macroscopic magnetic properties can be calculated. The bulk magnetic susceptibility (χ_m) is calculated using the usual statistical mechanics expression.[30] The value of g is 2.1 for **CuClMI**, as determined by EPR spectroscopy,[2] and, based on this, g = 2.1 is assumed for **CuBrMI** and **CuClPYR**. Note that all calculated magnetic data were compared to the experimental data.

Decomposition of J_{AB}

J_{AB} exchange interactions consist of physical components and can be decomposed into contributions from direct exchange (J_0), kinetic exchange (ΔJ_{KE}), core-electron polarisation (ΔJ_{CP}) and other exchange mechanisms (J_{Oth}) to yield eqn (2):

$$J_{AB} = J_0 + \Delta J_{KE} + \Delta J_{CP} + J_{Oth} \qquad (2)$$

In this scheme, J_0 describes the direct magnetic exchange between two Cu(II) ions, while ΔJ_{CP}, the core-polarisation exchange, describes the extent of spin polarisation of the MO's. ΔJ_{KE} indicates the kinetic exchange, which describes the extent to which unpaired electrons are delocalised, and J_{Oth} describes the contribution to the magnetic exchange from other sources.

These contributions to the J_{AB} magnetic exchange interaction were discovered through the use of advanced wave-function based methods.[31–34] The decomposition of J_{AB} is intrinsic to wave-function based methods,[35] and was also implemented in DFT based methods.[35,36] A recent implementation of this *J*-decomposition scheme was included in ORCA 4.0,[29] based on the work of Coulaud *et al.*[35,36]

J_{1T}, J_{1D} and J_{3T} were decomposed for **CuClMI**, **CuBrMI**, **CuClPYR**, **CuBrBA**, **CuClBA**, and compared to $Cu_2Cl_6^{2-}$.[35] These decomposition calculations were performed using RO-KSDFT (B3LYP, using def-2-QZVPP as the basis for Cu(II), while for all other atoms, SVP was used) in ORCA 4.2.0[29] at a convergence criteria of 1×10^{-9} Ha (VeryTightSCF). Convergence of the self-consistent field (SCF) required the following settings: ''Grid6 FinalGrid7'', ''DIISMaxEq 25'', ''directresetfreq 1'', and ''DecompositionPath Strict'' to obtain reliable singlet states. See ESI,† Section S4 for a full discussion.

Results and discussion

Crystallographic discussion of structures

To understand why FM interactions were reported for **CuClMI**,[2] the new structure of **CuBrMI** was determined in this study (see Table S1.1 (ESI†) for the crystallographic parameters of the two structures and Table S1.2 (ESI†) for selected bond lengths and angles in Section S1, ESI†). The two compounds di-chloro-*bis*[chloro(2-methyl-1,2-thiazol-3(2*H*)-one)copper(II)], **CuClMI**, and di-bromo-*bis*[bromo(2-methyl-1,2-thiazol-3(2*H*)-one)copper(II)], **CuBrMI**, are isostructural (see Fig. 2(a) and (b) for dimeric units). Comparison of **CuClMI** and **CuBrMI** reveals that the Cu–X bond lengths and X–Cu–X, Cu–X–Cu, X···Cu–X, and Cu···X–Cu angles are all similar. With similar geometries in

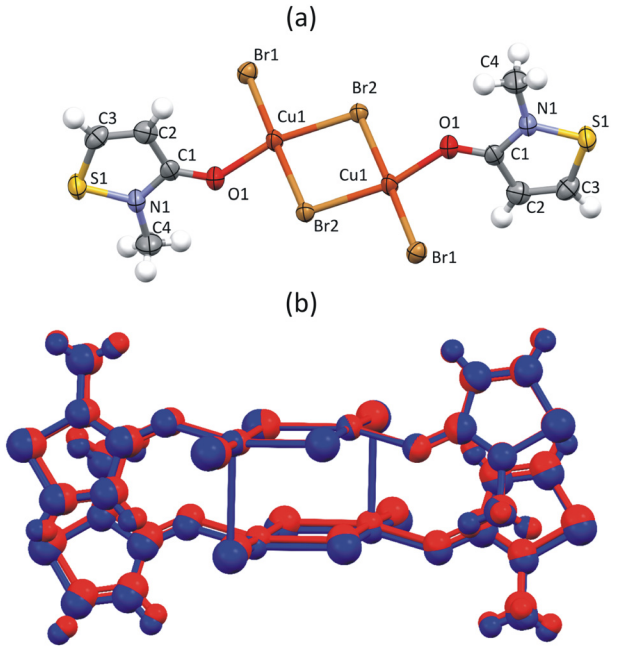

Fig. 2 Dimeric unit of (a) **CuBrMI**. Atoms are drawn at a 50% probability, while hydrogen atoms are drawn as spheres of arbitrary radii. (b) Overlap of two isostructural stacked dimers of **CuClMI** (red) and **CuBrMI**[2] (blue), plotted as a ball and stick representation.

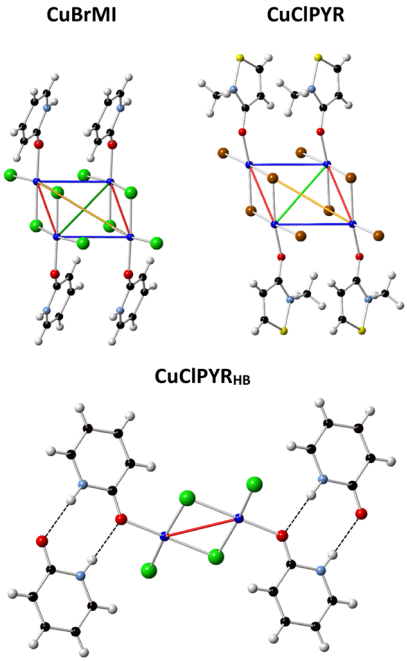

Fig. 3 Tetrameric finite cluster models used for **CuClMI**, **CuBrMI** and **CuClPYR** showing potential intra-dimer in-plane interactions J_1 to J_4. Coloured lines indicate the exchange interactions: J_1 (red), J_2 (blue), J_3 (green), and J_4 (orange). Atomic colors: Cu (blue), Cl (green), Br (brown), C (black), O (red), N (light blue), S (yellow) and H (white).

the dimers and polymers, similar magnetic properties are expected for the chloride and bromide analogues.

Assessing the nature of the magnetic interactions

A computational First-Principles Bottom-Up[11] FPBU study was completed for **CuClMI**, **CuBrMI** and **CuClPYR** to obtain an improved fundamental understanding of the magnetic behaviour of these amide-containing polymers. For brevity, most of the analysis of **CuClPYR** is documented in Section S5 (ESI†), while there is some additional discussion of **CuXMI** results given in Section S3 (ESI†). In the present study, nine potential pairs of radicals (d_1–d_9) were identified from the crystal structures of **CuClMI** and **CuBrMI**, and ten pairs for **CuClPYR**, up to a cut-off distance of ~10 Å between Cu(II) ions. Specifically, for **CuXL**, d_1 is the radical pair comprised of the Cu(II) ions in the $Cu_2(L)_2X_4$ (where L = MI, PYR or BA) dimeric unit, while the radical pair in d_2 contains fragments of two neighbouring stacked dimers along the polymer axis (see radicals connected by red and blue lines in tetramer model in Fig. 3, respectively). d_3 and d_4 involve the Cu(II) ions from two neighbouring dimeric units diagonally across the dimeric unit (in green and orange in tetramer model, see Fig. 3). The interactions d_1–d_4 are potential magnetic couplings within the 1D polymers, whereas d_5–d_{10} are potential interactions between the polymers. Since d_5–d_{10} are computed to have a very small J_{5-10} exchange interaction, their effect on the overall magnetic properties is small, as discussed in ESI,† Section S3, and will not be discussed here. Finite tetramer cluster models for both compounds were constructed from the crystal structures in such a way that the chemical environments around these square planar clusters are chemically representative of the environment around the Cu(II) ions (*i.e.* halides and L ligands coordinated to the Cu(II) ions, as shown in Fig. 3). For **CuClPYR**, each PYR ligand forms a hydrogen-bonded dimer with another PYR molecule from a neighbouring chain. To consider whether this hydrogen bond has an effect on the magnetic properties, the tetrameric structure, **CuClPYR$_{HB}$** was also considered (see Section S5, ESI†).

The magnetic exchange interaction in a radical pair d_i will be indicated by J_i. A tetrameric cluster containing four Cu(II) ions was used to calculate J_1–J_4, as shown in Fig. 3, using several different spin configurations. Dimer clusters consisting of only two Cu(II) ions were used to calculate J_5–J_{10}. The calculated magnitudes of J_1–J_4 are larger for **CuBrMI** than for **CuClMI** (see Table 2), which can be explained by the higher magnetic exchange through bromide ligands compared to chloride ligands.[6,9] For all compounds, the intra-dimer J_1 interaction

Table 2 Computed U-DFT J_i values for **CuClMI**, **CuBrMI** and two different models of **CuClPYR**. Note that for $J_{i,T}$, "T" refers to the tetramer model, while for **CuClPYR$_{HB}$**, the "HB" refers to a tetramer model with additional hydrogen bonded PYR molecules. With respect to Fig. 3, J_1 (red), J_2 (blue), J_3 (green), J_4 (orange)

	J_{1T}	J_{2T}	J_{3T}	J_{4T}
CuClBA	34.70	0.95	−6.22	1.21
CuClMI	33.51	0.61	−5.55	1.12
CuClPYR	11.67	1.11	0.36	0.10
CuClPYR$_{HB}$	19.26	0.82	0.52	0.09
CuBrMI	49.16	0.03	−6.09	0.09
CuBrBA	49.67	1.61	−10.79	2.16

is FM, with J_1 for **CuClPYR** significantly smaller than that of **CuClMI**.

The sign and magnitude of J_1 in these compounds (see Table 2) can be attributed to the significant orthogonal overlap of the singly occupied (SOMO) orbitals, in agreement with the Goodenough–Kannamori rules,[37,38] (see ESI,† Section S6) and agrees with previous findings for **CuClMI**[2] (J = +28.6 cm^{-1}) and other related compounds (*e.g.* +34.70 cm^{-1} for **CuClBA** and +49.67 cm^{-1} for **CuBrBA**).[6] For **CuClPYR** J_1 = +11.67 cm^{-1}, while the inclusion of the hydrogen-bonded pair almost doubles the value of J_1, highlighting the importance of including the broader chemical environment of a magnetic molecule when calculating the value of J interactions. **CuClPYR** has a surprisingly small value for J_1 compared to **CuClMI** and **CuClBA**, considering that the inorganic portions are very similar, and the organic ligands are all O-donor amides.

Due to the strength of J_1, the d_1 radical pair (which is the $Cu_2L_2X_4$ dimeric unit) can be considered as the magnetic building block of these compounds which form S = 1 dimers at low temperature. These primary building blocks are linked by three interactions, namely J_2, J_3 and J_4, and -depending on the strength of these secondary magnetic couplings- become either alternate links in a 1D chain magnetic topology or rungs in a 1D spin ladder topology. These interactions generally comprise short Cu···Cu, Cu–X···Cu, and Cu–X···X–Cu contacts that are potentially involved in the magnetic exchange between the $Cu_2L_2X_4$ building blocks.

J_2 is FM for **CuXL**, and involves two Cu–X_{cis}···Cu contacts, where X_{cis} refers to the halide ligand *cis* to MI/PYR. One interaction comprises the Cu–X_{cis}···Cu pathway involving the bridging halide ligand and another a Cu–X_{cis}···Cu pathway involving the terminal halide ligand. This asymmetry in the exchange would not be fully accounted for if using a dimer model (see ESI,† Section S2) because it does not account for the change in electron density on the bridging halide ligand. However, this effect is included in the tetramer model, where the bridging and terminal halide ligands are appropriately represented (see tetramer structures in Fig. 3) and explains why the tetrameric models generally perform better at estimating magnetic exchange interactions.[39]

The J_3 interaction of the MI and BA analogs are all AFM, while J_3 is FM for **CuClPYR**. The absolute magnitude of J_3 for **CuClPYR** is also significantly smaller than the other amides. Note that the geometries of the inorganic portions of **CuClL** are essentially the same, and therefore cannot explain why **CuClPYR** has a FM J_3 interaction, and the other amides have an AFM J_3 value. Thus, the organic ligand must be the cause of the observed differences in J_3. Since all the L-ligands are chemically similar O-donor amides, it is unlikely that PYR itself is the cause, and it is more probable that the orientation of PYR is the cause for the lower value of J_1, and for the FM J_3 value.

Based on these results, an AFM ground state is expected for **CuXMI**. This finding is in contrast to the experimental bulk FM properties reported previously for **CuClMI**.[2] A FM ground state is expected for **CuClPYR**, agreeing with previous experimental properties.[7]

Since an AFM ground state was predicted for **CuClMI**, a multitude of computational analyses were performed, including testing the effects of ligand exchange, magnetic field effects upon calculating the magnetic susceptibility, the effects of thermal contraction on J_3, and testing whether a small difference in the inter-dimer exchange could have produced a FM response (see ESI,† Section S7, for a detailed discussion). The tests demonstrated that the computational model and method used were indeed robust, and concluded that strong FM interactions occur between Cu(II) ions in the dimer and weak AFM interactions are calculated between dimers. This prompted a re-examination of the experimental magnetic properties of **CuClMI**, presented below.

Experimental magnetic results

Experimental data recorded for **CuClMI** in the current study agrees well, not only with the data recorded for the isostructural compound **CuBrMI** shown in Fig. 4(a)–(c), but also with exhaustive computational analyses, as mentioned in the previous section. Therefore, the magnetic susceptibility data recorded in the current study were used exclusively for further analysis of the magnetic properties of **CuClMI**.

$\chi_m(T)$ data were recorded on phase pure powder samples of **CuClMI** and **CuBrMI**, as documented in the Experimental section. The $\chi_m(T)$ data (Fig. 4(a)) show an increase in susceptibility to a maximum of 0.0815 emu Oe^{-1} mol^{-1} at 2.69 K and 0.026 emu Oe^{-1} mol^{-1} at 7.89 K for **CuClMI** and **CuBrMI**,

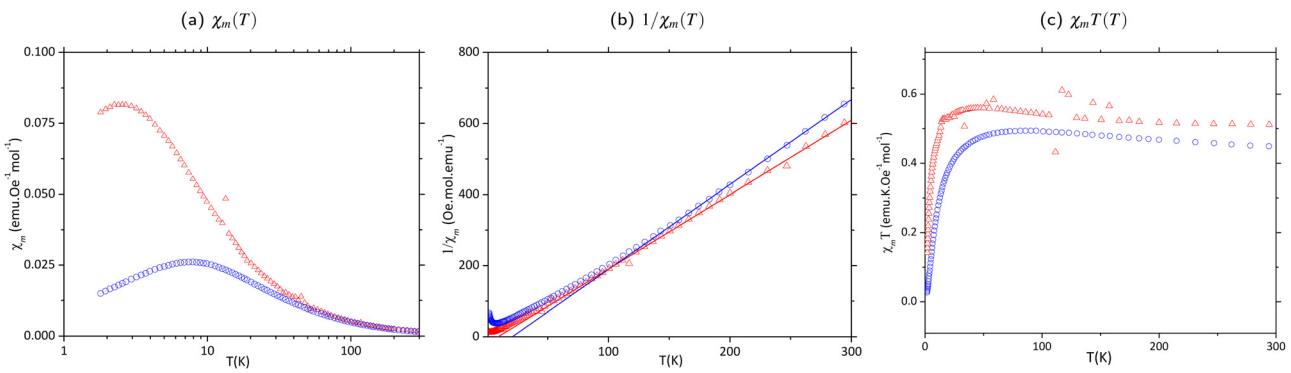

Fig. 4 Magnetic susceptibility plots for newly recorded data for **CuClMI** (Δ in red) and **CuBrMI** (O in blue), where (a) $\chi_m(T)$, (b) $1/\chi_m(T)$, and (c) $\chi_m T(T)$.

Table 3 Parameters obtained from fitting of the magnetic data to the Curie–Weiss law. C is the Curie constant and θ the Curie–Weiss temperature

	C^a	θ (K)	R^2
CuClMI	0.477(5)	9(2)	0.997
CuBrMI	0.418(1)	20.7(8)	0.999

[a] C is given in units of emu K Oe^{-1} mol^{-1}.

respectively. This is indicative of weak AFM interactions. The experimental data recorded in this study for **CuClMI** show that the bulk magnetic properties of **CuClMI** are AFM.

The $1/\chi_m T$ data, shown in Fig. 4(b), were fitted to a Curie Weiss model ($T > 150$ K) and indicate the presence of dominant FM interactions, as expected from the values of J_i magnetic couplings listed in Table 2. The large upward deviation from the Curie Weiss law around 100 K and 50 K for **CuBrMI** and **CuClMI**, respectively, is indicative of dominant FM interactions being present at this temperature. A Curie constant value of 0.477(5) emu K Oe^{-1} mol^{-1} was obtained from a Curie fit of the susceptibility data measured in this study for **CuClMI** and a value of 0.418(1) emu K Oe^{-1} mol^{-1} was found for **CuBrMI** (see Table 3).

The $\chi_m T$ product data recorded in the current study increase from 0.488 emu K Oe^{-1} mol^{-1} and 0.450 emu K Oe^{-1} mol^{-1} at room temperature to a maximum of 0.542 emu K Oe^{-1} mol^{-1} at 48 K and 0.494 emu K Oe^{-1} mol^{-1} at 86 K for **CuClMI** and **CuBrMI**, respectively (see Fig. 4(c)). This again indicates the presence of strong FM interactions, while the rapid decrease at lower temperatures indicates the presence of weaker AFM interactions.

The experimental magnetic data recorded for **CuClMI** in this study exhibited significant signal noise in the low-temperature region, which is evident in Fig. 4(c). Magnetic susceptibility data were recorded again for a second sample of **CuClMI** from the same batch with the same noise randomly appearing. An anomaly is observed in both of the **CuClMI** sample's χ_m data at ~15 K, which is evident as a small "hump" in the $\chi_m T$ product data, shown in Fig. 4(c). (Also see Fig. S8.1 in ESI,† Section S8). It is unclear what caused this, therefore, some additional testing is required to understand its origin. This anomaly is especially interesting, since a potential magnetic phase transition was also observed for **CuClBA** at ~45 K.[6]

The magnetic topology of CuXMI and CuClPYR

Taking into account all significant interactions, the magnetic topology of **CuClMI** and **CuBrMI** consists of FM J_1 dimers that are connected by AFM J_3 interactions, which then further couple through very weak competing FM and AFM interactions (J_2 and J_4) into a polymeric chain. Our calculations suggest the presence of an alternating magnetic chain with strong FM and weak AFM interactions, which can be considered to be well isolated from other chains, as there are no significant interactions between them (see Fig. 5(a) and Table 2). **CuClPYR** has FM dimers (rungs), with FM interactions along the polymer (rails) to form a FM spin ladder, with weak cross-rung interactions (see Fig. 5(b) and Table 2).

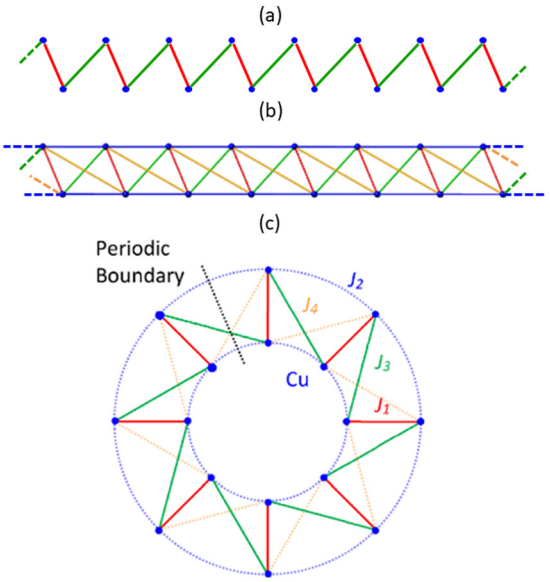

Fig. 5 (a) The 2 × 8 alternating chain for **CuClMI** and **CuBrMI**. (b) The 2 × 8 spin ladder model for **CuClPYR**. (c) General 2 × 8 cyclic model valid for all three compounds by switching off the appropriate J_i interactions. The cyclic model is constructed by mathematically connecting the ends of the 2 × 8 models. Interactions that cross the black periodic boundary condition are connected to the other end of the 2 × 8 model to introduce pseudo-periodic boundary conditions. Note that each **CuXL** moiety has been replaced by the Cu atom in blue. J_1 (red), J_2 (blue), J_3 (green), J_4 (orange).

After a comprehensive analysis of the performance of different potential open and cyclic magnetic models of **CuXL** with and without interactions between neighbouring polymeric chains (see ESI,† Section S3), it was concluded that the best magnetic model for calculating magnetic properties of **CuXMI** using statistical mechanics was a cyclic 16 Cu(II) cluster model using the J_i^{tetramer} (see Fig. 5(c)), which introduces pseudo periodic boundary conditions, while the 16 Cu(II) 2 × 8 model in Fig. 5(b) was best to calculate the magnetic susceptibility of **CuClPYR**. Note that the structure of **CuClPYR** was reported with an R-factor of 23%, so the quality of the calculated data is not as good, which is likely why the 2 × 8 model performed a bit better. For **CuBrMI**, the calculated temperature-dependent magnetic susceptibility shown in Fig. 6 predicts a maximum susceptibility of 0.031 emu Oe^{-1} mol^{-1} at 6.5 K (Exp: 0.026 emu Oe^{-1} mol^{-1} at 7.5 K) and correctly predicts an AFM ground state (see Section S3 (ESI†), for results obtained using other models). For **CuClMI**, the computational results replicated the experimental magnetic data recorded in this study. The calculated magnetic susceptibility as a function of temperature data predict a maximum in the susceptibility of 0.070 emu Oe^{-1} mol^{-1} at 3 K (Exp: 0.082 emu Oe^{-1} mol^{-1} at 2.69 K). Therefore, it correctly predicts an AFM ground state for **CuClMI** as shown in Fig. 6. For **CuClPYR**, the tetramer models with (red), and without (blue) additional hydrogen bonds both predict a FM ground state, with the inclusion of additional hydrogen-bonded molecules improving the estimation of the bulk magnetic susceptibility slightly with respect to the experimental data (black).

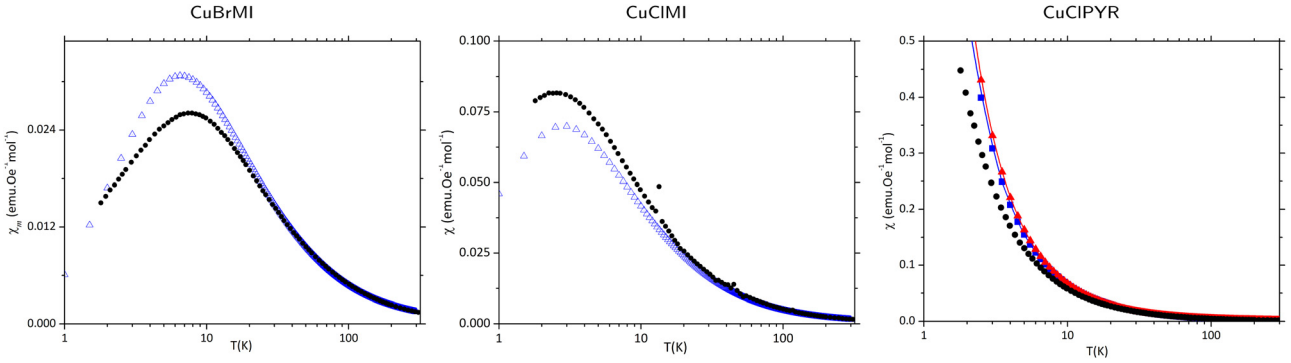

Fig. 6 Calculated $\chi_m(T)$ data for **CuBrMI** and **CuClMI**. Experimental (•) data, and calculated data (blue triangles) using a 2 × 8 cyclic model with J_{1T}. Calculated data of **CuClPYR** using the 2 × 8 model, for the hydrogen-bonded (solid blue triangles), and non-hydrogen-bonded (solid red triangles). Note that models are shown with interpolated data for clarity.

The macroscopic energy state population of **CuClMI** and **CuBrMI** at the temperature where the χ_m is at a maximum (T_{max}) reveals that many high spin states are responsible for the increase in the $\chi_m T$ product data at $T > T_{max}$ while at $T < T_{max}$ a singlet state becomes preferentially occupied, reducing χ_m at low temperature. This is discussed in more depth in Section S9 (ESI†). The high spin states at $T > T_{max}$ are due to FM coupling between Cu(II) ions in the dimers, with AFM interactions between the dimers resulting in the reduction of χ_m at low temperature. For **CuClPYR**, high spin states are more populated at low temperatures resulting in a FM ground state.

Satellite ligand effects on J_1 and J_3

The lower value of FM J_1 and the FM value of J_3 for **CuClPYR** are not due to the structure of the inorganic scaffolding, as they are essentially the same. Further, if these differences were caused by the type of ligand alone, then **CuClMI**, **CuClBA** and **CuClPYR** should have a similar effect on the J_1 and J_3 values. Instead, we find that **CuClMI** and **CuClBA** behave similarly to one another, and happen to have similar coordination torsion angles (Cl–Cu–O–C) of *ca.* 50°, while **CuClPYR** behaves differently, and has a coordination torsion angle of ~225°. Therefore, a study was carried out to assess the effect that this coordination torsion angle has on the magnetic exchange coupling between **CuXL** spin-carrying moieties.

The effect of rotation of the MI, BA, and PYR ligands about the Cu–O bond on the two main magnetic exchange interactions, namely J_1 and J_3, was examined using a dimer cluster which enables 360° rotation of the ligand and a tetramer model, respectively. The magnetic exchange interactions at some angles were also decomposed to examine how the individual components are affected by the rotation of the organic ligand MI, using the magnetic exchange decomposition scheme[40] as implemented in the software package ORCA.[29] Note that J_{1D} is generally 15% smaller than J_{1T}, but the compositions of J_{1D} and J_{1T} appear to be comparable. Let us remind here that, according to this scheme (eqn (2)), J_{AB} indicates the calculated magnetic exchange (namely, J_{1D} or J_{iT} with i = 1, 3) (see tetramer model in Fig. 3), J_0 describes the direct magnetic exchange between two Cu(II) ions, while ΔJ_{CP}, the core-polarisation exchange, describes the extent of spin polarisation of the MO's. ΔJ_{KE} indicates the kinetic exchange, which describes the extent to which unpaired electrons are delocalised, and J_{Oth} describes the contribution to the magnetic exchange from other sources.

Dimer rotation

The effect of the rotation of the MI, BA, and PYR ligands about the Cl–Cu–O–C torsion angle on the J_{1D} magnetic exchange interaction is shown in Fig. 7(a). At a torsion angle of 0° the amide plane is approximately co-planar with the Cu_2Cl_2 bridge plane, and at 90° the ligand is perpendicular to the inorganic bridge.

There is a major effect on J_{1D} upon rotation. Importantly, all three amides behave similarly, and this explains why the J_1 at the experimental positions (shown as larger solid symbols) is small for **CuClPYR**: the angle of the PYR in **CuClPYR** dampens the FM exchange across the dimer, but would result in an equal FM exchange to the other amides, if in a similar orientation (see blue line next to large solid orange and green symbols in Fig. 7(a)). To our knowledge, the effect of satellite orientation has not been reported before, with most of the focus being on either the bridge,[9] or the identity[10] of the terminal ligands.

While the three amides do behave similarly, there are some distinguishing features. **CuClBA** is distinct since it spans a larger range of values compared to the other two amides ($-40\ cm^{-1} < J < +50\ cm^{-1}$). J_{1D} is at a maximum when the ligand is at 0° (see Fig. 7(b), co-planar with the inorganic bridge, while all of the curves have a minimum at *ca.* 180°, which is interrupted by either a local maximum/peak shoulder. To understand these features, J_{1D} was decomposed and is illustrated as striped lines in ((Fig. 7(a))).

J_{1D}^{CuClMI} was decomposed at torsion angles of 0°, 54° (exp.), 140°, 180° and 225° (exp. value of **CuClPYR** at 135°–360° = −225°). From Table 4 it is clear that J_0, ΔJ_{CP}, and J_{Oth} remain relatively constant across the rotation, while the kinetic exchange ΔJ_{KE} varies greatly, as shown in Fig. 7. ΔJ_{KE} matches J_{1D}^{CuClMI} well, meaning that the rotation only appreciably affects ΔJ_{KE}.

In the case of $Cu_2Cl_6^{2-}$ (see Table 4),[35] there is significantly more delocalisation of spin density onto two terminal chloride

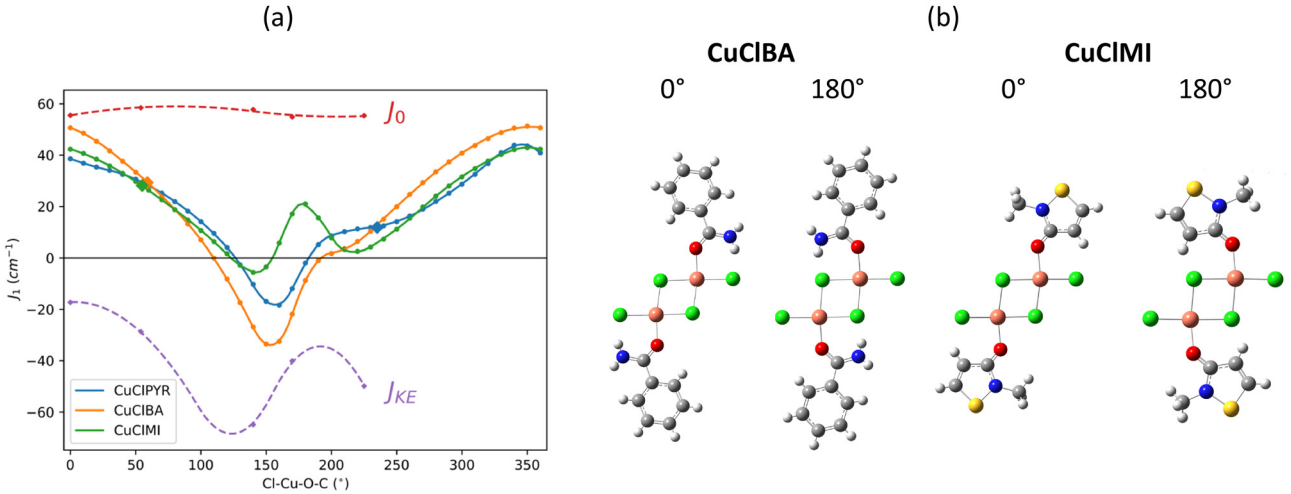

Fig. 7 (a) Magnetic exchange decomposition data for J_{1D} as a function of the Cl–Cu–O–C torsion angle with the values of J_{1D} calculated at the experimental structure shown as large solid diamond symbols. J_0 and J_{KE} refer to the decomposed J_{1D} for the various rotated **CuClMI** structures in Table 4. (b) Dimer structures of **CuClBA** and **CuClMI** at specific Cl–Cu–O–C angles.

Table 4 Decomposition of J_{1D} magnetic exchange interaction using dimer cluster models structures into its physical components. All values are given in units of cm^{-1}

Structure	J_{1D}	J_0	ΔJ_{KE}	ΔJ_{CP}	J_{Oth}
CuClMI(0°)	42.5	55.5	−17.3	7.3	−3.0
CuClMI(140°)	−5.0	57.8	−64.8	9.2	−7.1
CuClMI(180°)	21.0	54.4	−9.3	0.0	0.0
CuClMI(225°)	6.9	55.4	−49.9	8.3	−6.8
CuClMI	28.4	56.7	−31.7	7.9	−4.5
CuBrMI	42.3	70.4	−29.8	7.9	−6.2
CuClPYR	12.2	49.8	−39.6	7.2	−5.2
CuBrBA[6]	42.4	72.3	−31.6	7.9	−3.1
CuClBA[6]	29.7	55.6	−29.5	7.6	−2.0
$Cu_2Cl_6^{2-}$ [35 a]	−10.4	53.5	−70.3	6.5	

[a] $J_{1D}^{Cu_2Cl_6^{-2}}$ [35] was decomposed using a $Cu_2Cl_6^{2-}$ dimer (note values of original publication were divided by 2 to agree with Heisenberg Hamiltonian here used).

Table 5 Decomposition of J_{1T} and J_{3T} of **CuClMI**, **CuClMI(Rot)**, **CuClBA** and **CuClPYR** into their physical components. All values are given in units of cm^{-1}

J_i	J_i	J_0	ΔJ_{KE}	ΔJ_{CP}	J_{Oth}
J_{1T}^{CuClMI}	32.9	58.5	−28.7	8.1	−4.9
$J_{1T}^{CuClMI(Rot)}$	6.9	55.4	−49.9	8.3	−6.8
$J_{1T}^{CuClPYR}$	11.5	49.0	−39.7	7.2	−5.1
$J_{1T}^{CuClPYR_{HB}}$	18.9	53.5	−36.7	7.8	−5.7
J_{3T}^{CuClMI}	−2.5	1.2	−3.0	−0.3	−0.4
$J_{3T}^{CuClMI(Rot)}$	0.5	1.0	−0.1	−0.3	−0.1
$J_{3T}^{CuClPYR}$	2.0	3.1	−0.6	−0.2	−0.3
J_{3T}^{CuClBA}	−6.0	3.0	−7.3	−0.7	−0.9
$J_{2T}^{CuClMI(Rot)}$	0.57				
$J_{4T}^{CuClMI(Rot)}$	0.1				

The decomposition of J_{2T} and J_{4T} was not done due to their small magnitudes.

ligands, compared to the example shown here, which results in the massive ΔJ_{KE} overpowering J_0 to produce an AFM dimer.

The magnitude of J_{1D} is larger in **CuBrBA** and **CuBrMI**, compared to the chloride analogues. Magnetic exchange decomposition reveals that this is due to significantly larger direct exchange J_0, while ΔJ_{KE} is largely unaffected, and can be explained by the larger orbital overlap of μ-Br$^-$ with Cu(II), facilitating better direct exchange.

ΔJ_{KE}^{CuXBA} and ΔJ_{KE}^{CuXMI} are similar, irrespective of the X halide bridge. A terminal chloride ligand, on the other hand, results in a 2-fold increase of $\Delta J_{KE}^{Cu_2Cl_6^{-2}}$. From all of the evidence in this section, therefore, the terminal ligands exclusively modify the kinetic exchange, *via* their orientation and identity, while the identity of the bridging ligand affects the direct exchange exclusively.

Tetramer rotation

While J_1 is modulated by the orientation of the ligands, it is J_3 that determines whether a structure has a FM or AFM ground state. The values of J_{3D} were shown to be unreliable previously.[6] To obtain a more reliable decomposition of J_3, tetrameric clusters of **CuClMI**, **CuClBA**, **CuClPYR** were constructed. In addition, to illustrate that J_3 too is modulated by the orientation of the ligand, the MI ligand in **CuClMI** was rotated **CuClMI(Rot)** to match the torsional angle of the PYR ligand in **CuClPYR**, the results of which are given in Table 5.

The magnitude of $J_{1T}^{CuClMI(Rot)}$ is reduced by 80% upon rotation of MI, and matches the lower value of $J_{1T}^{CuClPYR}$ at the same angle. This is due to a large increase in kinetic exchange across the dimer, dampening the FM direct exchange. The inclusion of hydrogen-bonded molecules to the O-donor atom also has a significant effect on J_{1T}, and has an effect on both the kinetic and direct exchange components. This shows that the orientation of the ring, and weak interactions with non-magnetic molecules near the magnetic orbitals have a massive effect on the magnitude of J_1. Importantly, there is a reversal in the sign of $J_{3T}^{CuClMI(Rot)}$ to a weakly FM interaction. This matches the magnitude and sign of $J_{3T}^{CuClPYR}$, and shows that it is not the unique chemistry of PYR that

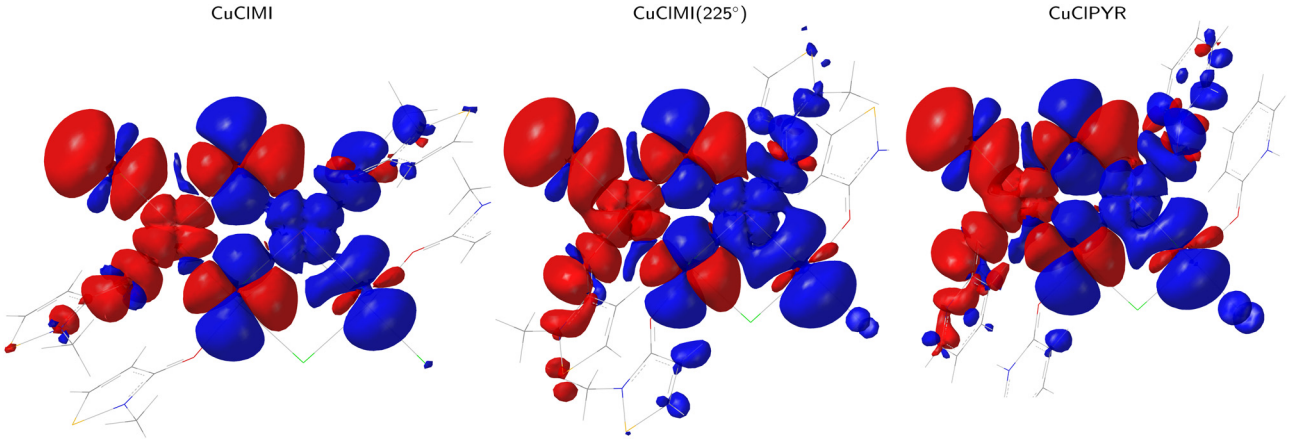

Fig. 8 Spin density difference of (BS,UFC) − (BS,RO) at various Cl–Cu–O–C torsion angles, which is a visual representation of ΔJ_{KE}.

causes the emergence of FM bulk properties, but it is simply a function of the angle at which the ligand is oriented, with respect to the magnetic orbitals. Decomposing J_{3T}^{CuClMI} and $J_{3T}^{CuClMI(Rot)}$ shows that the change from AFM to FM is again due to ΔJ_{KE}, which demonstrates that the orientation of the non-magnetic orbitals in the case of **CuClMI(Rot)** and **CuClPYR** allows a larger amount of spin density to delocalise from the magnetic orbitals. The real space representation of ΔJ_{KE} can be visualised by the spin density differences between the Broken-Symmetry Restricted Open-Shell $M_s = 0$ (BS,RO) solution and the Broken-Symmetry solution with the Unrestricted, but Frozen non-magnetic Core orbital solution, (BS,UFC), shown in Fig. 8. This means that when the MI ligand is at its experimental torsion angle of 54°, ($\Delta J_{KE} = -28.7$ cm^{-1}) the magnetic orbitals are confined to the O-, C-, and N-atoms, compared to when the angle is at 225°, ($\Delta J_{KE} = -49.9$ cm^{-1}) where the spin is allowed to relax further into MI, propagating onto the O-, C- N-, C_{Carb},- and S-atoms. **CuClPYR** beaves similarly to **CuClMI(Rot)**, with spin density propagating deep into the PYR ligand. Finally, let us mention that the local peaks at *ca.* 180° are due to opposite spin propagating into the portions of the ligand that is co-linear with the "opposite" Cu-μCl axis (shown as a blue volume in Fig. 8), reducing ΔJ_{KE}.

The manipulation of the terminal ligand can, therefore, lead to an alteration of the magnetic exchange in these materials, both in and between dimers. This means that isomorphs that have different ligand orientations can produce vastly different magnetic responses, and may even explain the anomaly observed for **CuClMI** at 15 K. In addition, ligand orientation disorder in structures, or doping can induce complex magnetic behavior. Finally, if the orientation of the rings can be manipulated *in situ*, a spin device can, in principle be constructed to flip between singlet/triplet states by just altering the orientation of the terminal ligand, for instance, by means of an electrical field as in the case of a prototypical biphenyl-based molecular system.[41]

Conclusions

The **CuBrMI** complex was structurally characterised and was found to be isostructural to the complex **CuClMI** reported in the literature.[2] The structures of the inorganic scaffolding of **CuClMI** and **CuBrMI** are essentially identical with slight differences due to different Cu–X bond lengths. Within the FPBU[11] strategy, the values of J_1 agree well with previous calculations for **CuClMI**[2] and are similar to those calculated for the benzamide analogue.[6] The inclusion of hydrogen-bonded molecules in **CuClPYR** was shown to significantly affect the magnetic exchange in the dimer.

The computed macroscopic magnetic susceptibility $\chi_m(T)$ curves of **CuXMI** agree excellently with the experimentally observed AFM behaviour of these compounds determined in this study, while the FM bulk properties of **CuClPYR** is, too, replicated well, especially if hydrogen-bonded molecules are added. The magnetic topology of **CuXMI** is described by alternating FM/AFM chains with limited FM NNN interactions, while **CuClPYR** is best described as a spin ladder with some cross-rung interactions.

The rotation of three amide-ligand dimers, extracted from **CuClPYR**, **CuClBA**, and **CuClMI**, shows that the magnetic interaction in, and between dimers can be modulated by the orientation of the ligands. Importantly, we showed that the FM properties of **CuClPYR** can be explained by the ligand's orientation, and would act similarly to other amides, if oriented similarly. Furthermore, it was shown through magnetic exchange decomposition that the identity, and orientation of the terminal/satellite ligands selectively affected the kinetic exchange in, and between dimers, while the bridging ligands only affect the direct exchange. This is due to the delocalization of spin density onto the terminal ligands to various degrees, which is dependent on the orientation of the ligand as well. When this parameter is targeted, the magnetic exchange of dimer pairs with terminal ligands can be tuned from AFM to FM by altering the coordination torsion angle.

The identity of the terminal ligand influences the amount of kinetic exchange, with terminal chloride ligands providing extensive delocalisation of magnetic orbitals which Rodríguez *et al.*[10] examined previously, along with terminal ammonia and terminal amine ligands. The terminal halide ligands produced AFM exchange across the dimers, while ammonia and amine ligands produced FM exchange. Their work focussed on

magnetic exchange in the dimer, while the identity of the terminal ligands *between* dimers is also presented here. This work also adds the amide ligand to the system, which indeed results in FM exchange in the dimer, and it is not very sensitive to structural differences beyond the carbonyl atom. Critically, the orientation of the terminal/satellite ligands is shown to affect the magnetic exchange in and between dimers. To the best of our knowledge, the effect of rotation of nonmagnetic ligands on magnetic exchange has not been shown, and the mechanism of this dependence was isolated to the kinetic exchange. This new information introduces an additional design tool to tune the magnetic exchange. The switch of magnetic exchange from FM to AFM is observed for the **CuClMI** system at a C–O–Cu–Cl angle of 225°, although it is very weakly AFM at that angle. It is possible that there exists a ligand system where the magnetic exchange in the dimer is switchable to produce a triplet or singlet state if the kinetic exchange of the ligand is stronger. This new discovery can lead to better control of magnetic exchange in molecules, or even allow for the manipulation of spin in quantum devices.

Conflicts of interest

There are no conflicts to declare.

Acknowledgements

The authors thank Dr F. Malan for assistance with crystallographic aspects. MR acknowledges financial support from the University of Pretoria and Sasol. SC acknowledges a PhD bursary from the National Research Foundation (Grant no: 81614), and funding of a research visit to the University of Barcelona by the University of Pretoria Postgraduate Study Abroad Program. MMT and CPL are grateful for funds from PCI Synthesis, Inc. (now SEQENS) toward the purchase of the D8 Focus diffractometer, from the National Science Foundation (IMR-0314773) for purchase of the MPMS SQUID magnetometer, and from the Kresge Foundation for both instruments. MD and JJN thank the financial support from the Spanish Ministerio de Economía y Competitividad (Project No. PID2020-117803GB-I00 and CTQ2017-87773-P/AEI/FEDER), Spanish Structures of Excellence María de Maeztu program through grants MDM-2017-0767/CEX2021-001202-M, and Generalitat de Catalunya (Project No. 2017 SGR 348 and 2021 SGR 354). The authors thank the Institute of Theoretical and Computational Chemistry of the Universitat de Barcelona (IQTCUB) and the Centre for High-Performance Computing of South Africa (CHPC) for the use of their computational resources.

References

1 G. Givaja, P. Amo-Ochoa, C. J. Gómez-García and F. Zamora, *Chem. Soc. Rev.*, 2012, **41**, 115–147.
2 M. Kato, K. Hida, T. Fujihara and A. Nagasawa, *Eur. J. Inorg. Chem.*, 2010, 495–502.
3 C. Liu, D. R. Talham, J.-H. Park, E. Cizmar and M. W. Meisel, *J. Chem. Phys.*, 2004, **120**, 1140–1141.
4 S. N. Herringer, A. J. Longendyke, M. M. Turnbull, C. P. Landee, J. L. Wikaira, G. B. Jameson and S. G. Telfer, *Dalton Trans.*, 2010, **39**, 2785–2797.
5 C. P. Landee and M. M. Turnbull, *Eur. J. Inorg. Chem.*, 2013, 2266–2285.
6 S. Coetzee, M. M. Turnbull, C. P. Landee, J. J. Novoa, M. Deumal, S. Vela and M. Rademeyer, *Polyhedron*, 2020, **185**, 114603.
7 K. C. Shortsleeves, M. M. Turnbull, C. B. Seith, E. N. Tripodakis, F. Xiao, C. P. Landee, L. N. Dawe, D. Garrett, G. D. de Delgado and B. M. Foxman, *Polyhedron*, 2013, **64**, 110–121.
8 M. G. Banks, R. K. Kremer, C. Hoch, A. Simon, B. Ouladdiaf, J.-M. Broto, H. Rakoto, C. Lee and M.-H. Whangbo, *Phys. Rev. B: Condens. Matter Mater. Phys.*, 2009, **80**, 024404.
9 O. Castell, J. Miralles and R. Caballol, *Chem. Phys.*, 1994, **179**, 377–384.
10 A. Rodrìguez-Fortea, P. Alemany, S. Alvarez and E. Ruiz, *Inorg. Chem.*, 2002, **41**, 3769–3778.
11 J. J. Novoa, M. Deumal and J. Jornet-Somoza, *Chem. Soc. Rev.*, 2011, **40**, 3182.
12 F. H. Allen and C. R. Groom, *Angew. Chem., Int. Ed.*, 2014, **53**, 662–671.
13 Bruker, *SAINT+*, Bruker AXS Inc., Madison, Wisconsin, USA, 2012.
14 Bruker, *SADABS*, Bruker AXS Inc., Madison, Wisconsin, USA, 2001.
15 Bruker, *APEXII*, Bruker AXS Inc., Madison, Wisconsin, USA, 2012.
16 G. M. Sheldrick, *Acta Crystallogr., Sect. A: Found. Crystallogr.*, 2008, **64**, 112–122.
17 L. J. Farrugia, *J. Appl. Crystallogr.*, 2012, **45**, 849–854.
18 G. M. Sheldrick, *Acta Crystallogr., Sect. C: Struct. Chem.*, 2015, **71**, 3–8.
19 C. F. Macrae, P. R. Edgington, P. McCabe, E. Pidcock, G. P. Shields, R. Taylor, M. Towler and J. van de Streek, *J. Appl. Crystallogr.*, 2006, **39**, 453–457.
20 D. C. Palmer, *Z. Kristallogr.-Crys. Mater.*, 2015, **230**, 559–572.
21 V. Vreshch, *J. Appl. Crystallogr.*, 2010, **44**, 219–220.
22 L. Noodleman, *J. Chem. Phys.*, 1981, **74**, 5737–5743.
23 A. D. Becke, *J. Chem. Phys.*, 1993, **98**, 5648–5652.
24 C. Lee, W. Yang and R. G. Parr, *Phys. Rev. B: Condens. Matter Mater. Phys.*, 1988, **37**, 785–789.
25 S. H. Vosko, L. Wilk and M. Nusair, *Can. J. Phys.*, 1980, **58**, 1200–1211.
26 P. J. Stephens, F. J. Devlin, C. F. Chabalowski and M. J. Frisch, *J. Phys. Chem.*, 1994, **98**, 11623–11627.
27 A. Schafer, H. Horn and R. Ahlrichs, *J. Chem. Phys.*, 1992, **97**, 2571–2577.
28 M. J. Frisch, G. W. Trucks, H. B. Schlegel, G. E. Scuseria, M. A. Robb, J. R. Cheeseman, G. Scalmani, V. Barone, B. Mennucci, G. A. Petersson, H. Nakatsuji, M. Caricato, X. Li, H. P. Hratchian, A. F. Izmaylov, J. Bloino, G. Zheng, J. L. Sonnenberg, M. Hada, M. Ehara, K. Toyota, R. Fukuda,

J. Hasegawa, M. Ishida, T. Nakajima, Y. Honda, O. Kitao, H. Nakai, T. Vreven, J. A. Montgomery Jr., J. E. Peralta, F. Ogliaro, M. Bearpark, J. J. Heyd, E. Brothers, K. N. Kudin, V. N. Staroverov, R. Kobayashi, J. Normand, K. Raghavachari, A. Rendell, J. C. Burant, S. S. Iyengar, J. Tomasi, M. Cossi, N. Rega, J. M. Millam, M. Klene, J. E. Knox, J. B. Cross, V. Bakken, C. Adamo, J. Jaramillo, R. Gomperts, R. E. Stratmann, O. Yazyev, A. J. Austin, R. Cammi, C. Pomelli, J. W. Ochterski, R. L. Martin, K. Morokuma, V. G. Zakrzewski, G. A. Voth, P. Salvador, J. J. Dannenberg, S. Dapprich, A. D. Daniels, O. Farkas, J. B. Foresman, J. V. Ortiz, J. Cioslowski and D. J. Fox, *Gaussian ~ 09 Revision D.01*, 2009.

29 F. Neese, *Wiley Interdiscip. Rev.: Comput. Mol. Sci.*, 2018, **8**, e1327.

30 O. Kahn, *Molecular Magnetism*, VCH, 1993.

31 T. Terencio, R. Bastardis, N. Suaud, D. Maynau, J. Bonvoisin, J. P. Malrieu, C. J. Calzado and N. Guihery, *Phys. Chem. Chem. Phys.*, 2011, **13**, 12314–12320.

32 C. J. Calzado, C. Angeli, D. Taratiel, R. Caballol and J.-P. Malrieu, *J. Chem. Phys.*, 2009, **131**, 044327.

33 C. J. Calzado, J. Cabrero, J. P. Malrieu and R. Caballol, *J. Chem. Phys.*, 2002, **116**, 2728–2747.

34 C. J. Calzado, J. Cabrero, J. P. Malrieu and R. Caballol, *J. Chem. Phys.*, 2002, **116**, 3985–4000.

35 E. Coulaud, J.-P. Malrieu, N. Guihery and N. Ferre, *J. Chem. Theory Comput.*, 2013, **9**, 3429–3436.

36 E. Coulaud, N. Guihery, J.-P. Malrieu, D. Hagebaum-Reignier, D. Siri and N. Ferre, *J. Chem. Phys.*, 2012, **137**, 114106.

37 J. B. Goodenough, *Phys. Rev.*, 1955, **100**, 564–573.

38 J. Kanamori, *J. Phys. Chem. Solids*, 1959, **10**, 87–98.

39 S. Vela, A. Sopena, J. Ribas-Arino, J. J. Novoa and M. Deumal, *Chem. – Eur. J.*, 2014, **20**, 7083–7090.

40 G. David, F. Wennmohs, F. Neese and N. Ferr, *Inorg. Chem.*, 2018, **57**, 12769–12776.

41 K. Jutglar Lozano, R. Santiago, J. Ribas-Arino and S. T. Bromley, *Phys. Chem. Chem. Phys.*, 2021, **23**, 3844–3855.